Accepted Manuscript of: *Hoffmann, C., Weigert, J., Esche, E., & Repke, J.-U. (2019). Towards Demand-side Management of the Chlor-alkali Electrolysis: Dynamic, Pressure-driven Modeling and Model Validation of the 1,2-Dichloroethane Synthesis. Chemical Engineering Science, 115358. https://doi.org/10.1016/j.ces.2019.115358*

Towards Demand-side Management of the Chlor-alkali Electrolysis: Dynamic, Pressure-driven Modeling and Model Validation of the 1,2-Dichloroethane Synthesis

Christian Hoffmann[a,*], Joris Weigert[a], Erik Esche[a], Jens-Uwe Repke[a]

[a]*Technische Universität Berlin, Process Dynamics and Operations Group, Sekr. KWT 9, Straße des 17. Juni 135, Berlin 10623, Germany*

Abstract

A promising application of demand-side management is the chlor-alkali electrolysis. However, storing the produced chlorine for flexibility should be avoided whenever possible. If PVC is produced from chlorine, storing the intermediate 1,2-dichloroethane resulting from direct chlorination of ethene is a better alternative as it is less toxic than chlorine and can be easily stored. Currently, no dynamic process models to study the process behavior or to develop optimal trajectories for the 1,2-dichloroethane production under different demand response scenarios are available. Hence, we formulate and solve a dynamic, pressure-driven model of the synthesis of 1,2-dichloroethane and validate it with real process data in this contribution. As part of this dynamic model, differentiable formulations for weeping and the flow over a weir of a distillation tray are presented, which are also valid whenever certain trays run dry.

Keywords: Dynamic pressure-driven modeling, Chloralkali electrolysis, Ethylene dichloride, Plant flexibilization

1. Introduction

The share of renewable energy in the electricity market is increasing in countries all over the world [1]. This is desirable for many reasons, such as reduced

*Corresponding author
Email addresses: c.hoffmann@tu-berlin.de (Christian Hoffmann), joris.weigert@tu-berlin.de (Joris Weigert), erik.esche@tu-berlin.de (Erik Esche), j.repke@tu-berlin.de (Jens-Uwe Repke)

CO_2 emissions, less dependence on crude oil and natural gas, long-term sustainability, or decentralized energy solutions. On the other hand, it raises new technical challenges, e.g. net stability for fluctuating energy input and availability. Finding solutions to these challenges is an important task for the process industry and demand-side management (DSM) with flexible plant operation is expected to be an important aspect [2, 3]. In particular, companies with energy-intensive processes have a large potential for such approaches [4]. According to Ausfelder et al. [4], the chlor-alkali electrolysis (CAE) has the highest flexibility potential in the chemical industry due to the large installed capacity of more than 1 GW in Germany [5, 6, 4].

The main product of the CAE is chlorine gas (Cl_2), which is obtained at the anode of the electrolyzer. The CAE has been modeled dynamically in the past [7] and also recently for demand response purposes [8, 9]. Otashu and Baldea [8] used a dynamic model of the CAE for demand-side management. They showed that CAE can be used for DSM, but several variables including the cell temperature must be carefully controlled during load transitions. Brée et al. [9] compared a standard cathode with an oxygen depolarized cathode by solving a mixed-integer linear programming problem and showed that the standard cathode is currently economically superior to the oxygen depolarized one, but this may change in the future. They also pointed out that storing chlorine for flexibility purposes should be avoided whenever possible [9].

Approximately 30 % of the chlorine produced around the world are processed to 1,2-dichloroethane (typically known as ethylene dichloride or EDC) and further to polyvinyl chloride (PVC) [10][1], a thermoplastic polymer mainly used for construction, domestic use, packaging, and transport [11]. EDC has several advantageous properties regarding the flexibilization of the process. It can be easily stored in the liquid state, is less toxic than chlorine and chemically stable. Hence, using an EDC storage tank is a valid alternative to chlorine storage for a relatively large amount of the processed chlorine and has been assigned a technical flexibility potential for load reduction of 10 % [4]. There is no positive potential as the storage must be refilled and CAE plants operate close to maximum capacity [6].

Up to now, no dynamic models of the EDC production have been published. A dynamic process model is preferred as Sass and Mitsos [12] recently showed that the inherent dynamics of the system may play a significant role and that quasi-steady models do only perform well with adequate ramp constraints. For this

[1] if one considers that part of the chlorine is recycled for the oxychlorination, see Section 2

reason, we present a dynamic model to assess the transient behavior of the EDC synthesis. This model will be used to assess the challenges and limitations during operation and for different loads, to predict the process behavior, and to obtain optimal trajectories from one setpoint to another. Due to the limited number of publications in the literature, e.g. [13], this model development includes the selection of a thermodynamic model and a review of the available reaction kinetics.

In the following, we assume inlet flows of chlorine from the CAE and ethene as given and focus on the model development for the EDC production. The next section introduces the fundamentals of the VCM production and shows the parts of the process subject to flexibilization. Section 3 discusses the process model for these parts, whereas section 4 presents a case study to illustrate the modeling approach and presents steady-state and dynamic simulation results. These results are compared to real process data for model validation.

2. Process Description and Modeling Approach

VCM is typically produced in an integrated plant where ethene (C_2H_4) is partly directly chlorinated and partly oxychlorinated [14, p. 10], as shown in Figure 1. The chlorine for direct chlorination stems from the CAE. In both reaction steps, EDC is produced and then purified to remove byproducts. Afterwards, EDC is cracked to produce VCM. During the purification of VCM, hydrogen chloride (HCl) is removed and recycled back to the oxychlorination. A scheme of the process is given in Figure 1.

As EDC can be stored easily, the process could be made flexible by adding a storage tank to the flowsheet. In case of electricity shortages or high electricity costs, this tank is used to ensure the continuous operation of the following units. In the opposite case, the tank is filled. This way, oxychlorination, EDC cracking, and VCM purification always operate at nominal operating conditions while direct chlorination and EDC purification must dynamically follow the chlorine feed. The boundary between flexibly operated units and units at nominal operating conditions is highlighted with a dashed line in Figure 1. As direct chlorination and EDC purification shall be operated flexibly, these two units are discussed in more detail to convey a better understanding of the process model in section 3.

In the direct chlorination process, ethene and chlorine are usually reacted in the liquid phase consisting mainly of the product EDC in the presence of a Lewis acid catalyst, such as $FeCl_3$ [14, p. 10]. Equation (1) is the main reaction in which ethene and chlorine react to EDC. Equation (2) is the side reaction of EDC and chlorine to the byproducts 1,1,2-trichloroethane (ETC, $C_2H_3Cl_3$) and hydrogen

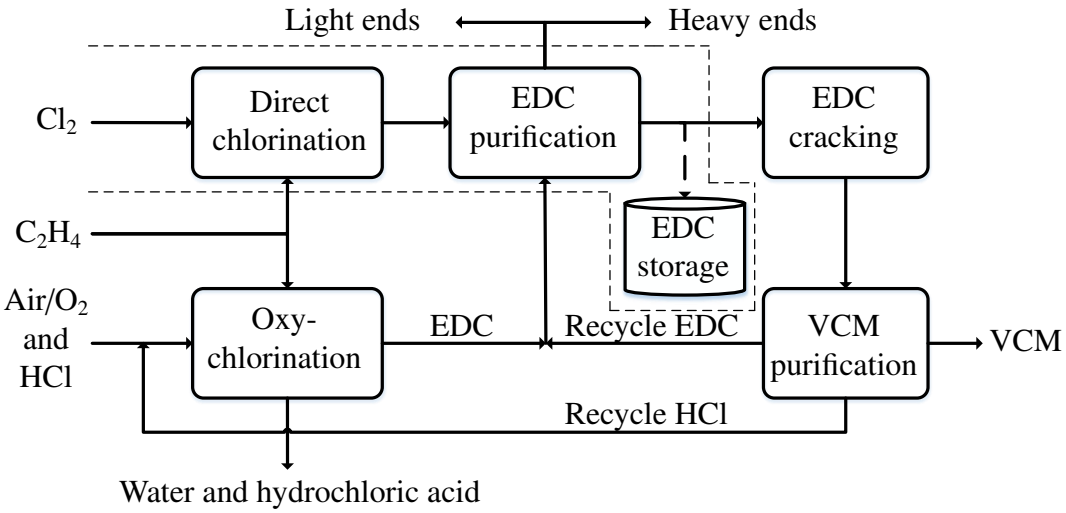

Figure 1: Process scheme of an integrated VCM production plant, based on [14, p. 36]. The dashed line represents the boundary between flexibly operated units and units operating at nominal conditions.

chloride (HCl):

$$C_2H_4 + Cl_2 \longrightarrow C_2H_4Cl_2 \tag{1}$$

$$C_2H_4Cl_2 + Cl_2 \longrightarrow C_2H_3Cl_3 + HCl \tag{2}$$

In principal, there are two options for direct chlorination: low-temperature chlorination (LTC) and high-temperature chlorination (HTC) [14, p. 11], which are operated at ambient pressure and high conversion rates. In the first case, low temperatures (20 to 70 °C) lead to higher selectivities ($\geq$ 99 %) but increased energy demand. In the second case, the heat of reaction is used for EDC purification in a distillation process as the heat of reaction is about seven times larger than EDC's heat of vaporization [14, p. 11]. While the increased temperatures of 85 to 200 °C conventionally led to lower selectivity, current patents claim this not longer to be true if highly selective catalysts are applied. For this reason, LTC is hardly built anymore [15].

In this contribution, the latter case is modeled and the reactor is thus placed directly below the distillation tower, as shown in [14, p. 11]. The distillation tower is assumed to be a tray column. In addition, we consider a heat exchanger located below the reactor to remove additional heat as described in Kahsnitz and Polte [15]. This assumed process design is shown in Figure 2, where the control volumes of the process model are also indicated (see section 3).

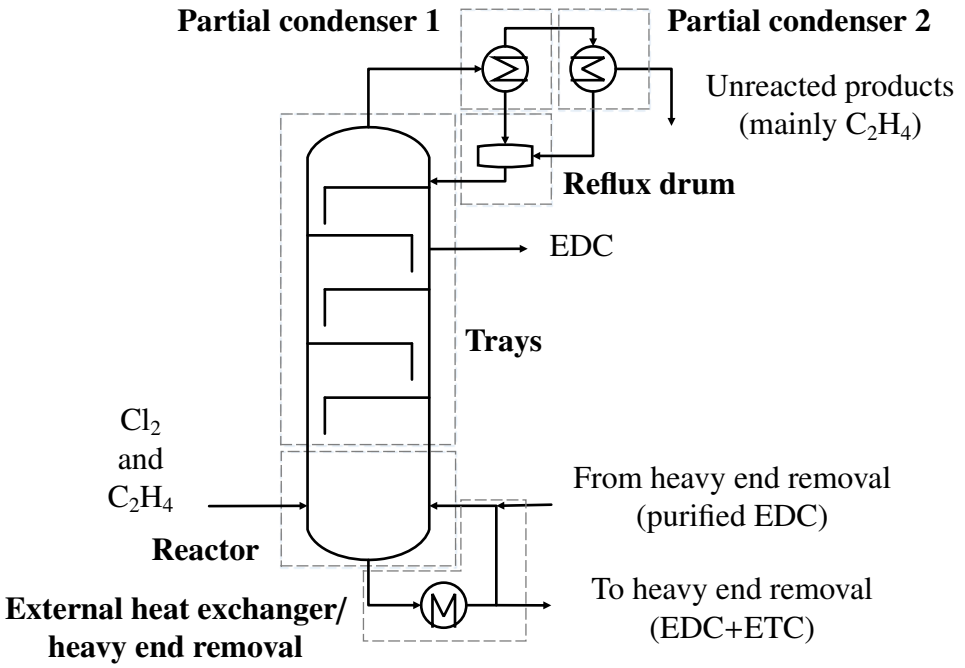

Figure 2: Assumed process design for direct chlorination and EDC purification, based on [14, p. 11]. Also shown are the parts of the process model, see section 3.

3. Process Modeling

In this section, the process model is developed. The first step is the determination of an appropriate thermodynamic model. Afterwards, the kinetics of the process are discussed. Finally, the model equations of each unit are introduced.

3.1. Thermodynamics

This section discusses the thermodynamic models used to describe pure component data as well as the mixtures thereof. Both the Soave-Redlich-Kwong (SRK) equation of state (EoS) and the Peng-Robinson (PR) equation of state were tested for this system [16, 17]. Better results were obtained with the latter. Hence, only the PR EoS will be discussed in the following.

3.1.1. Pure Components

To test the applicability of the PR EoS, its ability to describe the pure components was checked first by comparing its predictions with fitted empirical equations for vapor pressure, saturated liquid density, and the enthalpy of vaporization. These empirical equations are assumed to be the ground truth and the quality of the PR EoS is evaluated against them. As the temperature range of the plant operation is 298 to 423 K, all graphs are limited to this interval.
The PR EoS employed here consists of the following equations

$$P = \frac{RT}{v-b} - \frac{a}{v^2 + 2bv - b^2}\,, \tag{3}$$

$$a = 0.457235\,\frac{(RT_C)^2}{P_C}\,\alpha(T)\,, \tag{4}$$

$$b = 0.077796\,\frac{RT_C}{P_C}\,, \tag{5}$$

$$\alpha = \left(1 + m\left(1 - \sqrt{\frac{T}{T_C}}\right)\right)^2\,, \tag{6}$$

$$m = 0.37464 + 1.54226\omega - 0.26992\omega^2\,, \tag{7}$$

where T_C and P_C are the critical temperature and pressure, and ω is the acentric factor. These three parameters for each component are taken from [18].
As shown in the parity plots in Figure 3a to 3e, all three properties can be well described for EDC in the temperature range from 298 to 423 K. The error between experiment and equation of state is typically below 5 % indicated by the black, continuous lines. Only for lower temperatures, the error in the vapor pressure is

up to 10 % at low temperatures. Figure 3b, 3d, and 3f show the parity plots for ETC. Both vapor pressure and enthalpy of vaporization always show a deviation smaller than 5 %. The error in the liquid density is less than 7 %.
The other three components were also carefully checked and demonstrate a reasonable accuracy. Vapor pressure accuracy is always within ± 5 % while larger devations of more than 15 % for liquid density and enthalpy of vaporization are observed. However, their pure component vapor-liquid equilibria are not within the temperature range at which the plant operates.

3.1.2. Binary Mixtures

The PR EoS mixture formulation employed here reads:

$$P = \frac{RT}{v_{mix} - b_{mix}} - \frac{a_{mix}}{v_{mix}^2 + 2b_{mix}v_{mix} - b_{mix}^2} \tag{8}$$

$$a_{mix} = \sum_{c}\sum_{caux} x_c x_j a_{c,caux}, \quad a_{c,caux} = \sqrt{a_c a_{caux}}\,(1 - k_{c,caux}) \tag{9}$$

$$b_{mix} = \sum_{c} x_c b_c\,, \tag{10}$$

where we apply conventional mixing rules and $k_{c,caux}$ is the binary interaction parameter. Unfortunately, experimental data of the most important binary subsystems ethene/EDC and chlorine/EDC is scarce. This is the most important reason why we use an equation of state as they are more reliable when extrapolating from the available data. The binary interaction parameter is fitted to the available experimental data and is assumed to be temperature-independent. The binary interaction parameter for the remaining subsystems is set to zero.
The results for the binary systems ethene/EDC and chlorine/EDC are shown in Figure 4. Both binary systems can be accurately described with the PR EoS and standard mixing rules. The small deviation of the binary interaction parameter also indicates that the applied mixing rules are appropriate for the systems at hand. The other binary systems are modeled with a binary interaction parameter of zero due to the following reasoning: ETC and HCl are expected to only appear in small concentrations, hence the influence on the mixture should be negligible. In addition, experimental results showed that EDC and ETC form an ideal solution [19, 20], which is also predicted by the PR EoS.

3.2. Kinetics

There are three different kinetic models for the reactions in Eq. (1) and (2) available in the literature. Szépvölgyi and Ujhidy [22] and Orejas [13] consider

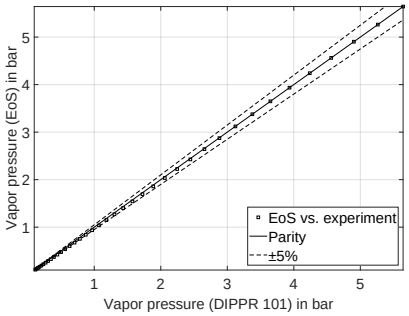

(a) Comparison of PR and DIPPR 101, parameters from [18, p. 2-56].

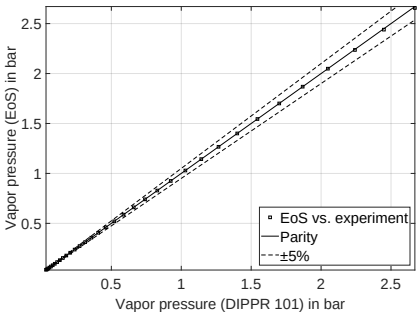

(b) Comparison of PR and DIPPR 101, parameters from [18, p. 2-60].

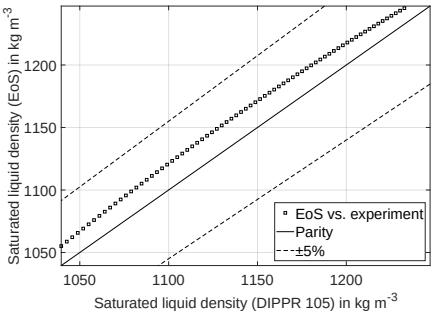

(c) Comparison of PR and DIPPR 105, parameters from [18, p. 2-99].

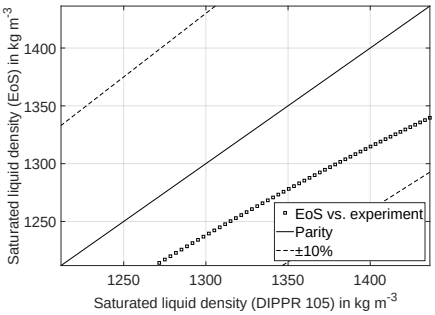

(d) Comparison of PR and DIPPR 105, parameters from [18, p. 2-103].

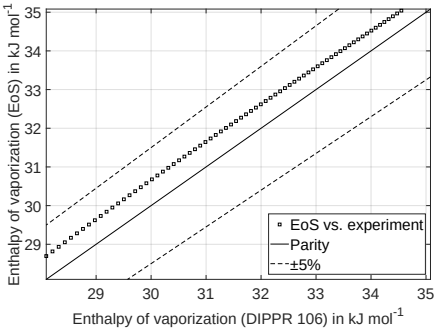

(e) Comparison of PR and DIPPR 106, parameters from [18, p. 2-151].

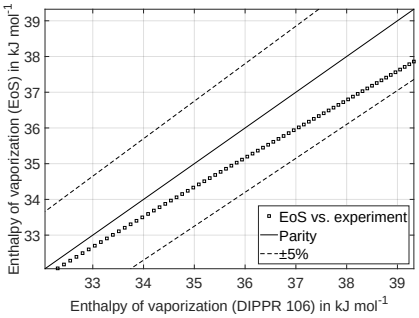

(f) Comparison of PR and DIPPR 106, parameters from [18, p. 2-155].

Figure 3: Parity plots for EDC (left) and ETC (right) in the temperature range from 298 to 423 K. The DIPPR equation is assumed to represent the true data.

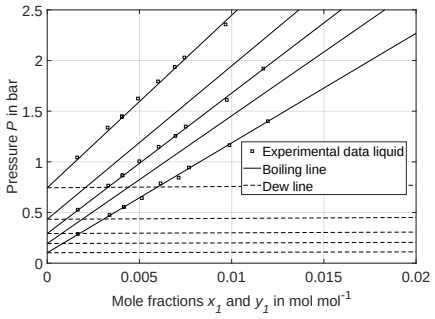

(a) P-x-y diagrams of ethene (1) and EDC (2) at 299.2, 313.15, 323, 333.15, and 348.4 K, $k_{12} = 0.0347$.

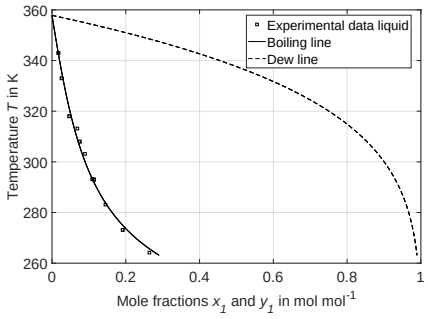

(b) T-x-y diagrams of chlorine (1) and EDC (2) at 1.013 25 bar, $k_{12} = 0.0336$.

Figure 4: Binary VLEs of ethene/EDC and chlorine/EDC. Experimental data from the Detherm database [21].

both reactions and use the following reaction rates with differing parameterization:

$$r_1 = k_1 \exp\left(-\frac{E_1}{RT}\right) c_{C_2H_4} c_{Cl_2} \tag{11}$$

$$r_2 = k_2 \exp\left(-\frac{E_2}{RT}\right) c_{C_2H_4} c_{Cl_2}^2 \,. \tag{12}$$

Wachi and Morikawa [23] only consider the main reaction. However, as ETC is found in real industrial plants, the second reaction cannot be neglected. Consequently, the kinetics by Wachi and Morikawa [23] were discarded in this work. Since there are no further independent experimental studies in the literature to the best of our knowledge, both remaining parameter sets were implemented. In general, the parameters from Szépvölgyi and Ujhidy [22] yield higher reaction rates than those by Orejas [13]. Both parameter set show an offset to the real plant (see section 4.2.1). Therefore, only the newer parameter set by Orejas [13] is used in the remainder of this work.

3.3. Model Equations

In the following paragraphs, the essential model equations describing the condensers, the reflux drum, the trays, the reactor, and the external heat exchanger are discussed. The whole model is available as supplementary material. The component indices throughout this work are given in Table 1. In addition, we start counting the trays at the top (condenser: $tr = 0$). Note that the model is formulated in terms of component flows. Mole fractions of components are only

calculated in post processing. This explains the unusual expressions, see e.g. the phase equilibrium.

Table 1: Component indices.

Index c	Component
1	C_2H_4
2	Cl_2
3	EDC
4	ETC
5	HCl

3.3.1. Condenser 1 and 2

The first condenser is assumed to be at steady-state due to the smaller hold ups and expected temperature changes compared to the rest of the plant:

Component and energy balances:

$$0 = F^V_{tr=1,c} - F^L_{\mathrm{CON},c} - F^V_{\mathrm{CON},c} \tag{13}$$

$$0 = Q_{\mathrm{CON}} + F^V_{tr=1} \cdot h^V_{tr=1} - F^L_{\mathrm{CON}} \cdot h^L_{\mathrm{CON}} - F^V_{\mathrm{CON}} \cdot h^V_{\mathrm{CON}} \tag{14}$$

The calculation of the vapor enthalpies and the enthalpy of vaporization is explained for all control volumes in section 3.3.6. The second condenser is modeled in analogy to the first, only the indices are changed.

3.3.2. Reflux drum

The model of the reflux drum contains dynamic mole balances. An energy balance is neglected, because the liquid is subcooled and small changes in the liquid holdup have only a small temperature influence.

Component balance:

$$\frac{\mathrm{d}HU_{\mathrm{RD},c}}{\mathrm{d}t} = F^L_{CON,c} + F^L_{\mathrm{CON2},c} - F^L_{tr=0,c}. \tag{15}$$

Ideal mixing:

$$HU_{\mathrm{RD},c} \cdot F^L_{tr=0} = \sum_{c=1}^{NC} HU_{\mathrm{RD},c} \cdot F^L_{tr=0,c}. \tag{16}$$

Volume:

$$\sum_{c=1}^{NC} HU_{\mathrm{RD},c} \cdot M_c = V_{\mathrm{RD}}^L \cdot \rho_{\mathrm{CON}}^L. \tag{17}$$

Volume correlation: The relation between volume and level of a horizontal cylinder is quite nonlinear; it contains an arccos function and a root. A more robust form of this equation is the approximation of this function with a cubic polynomial, in which the coefficients p_i must be fitted to the actual geometry:

$$V_{\mathrm{RD}}^L = p_1 \cdot (L_{\mathrm{RD}})^3 + p_2 \cdot (L_{\mathrm{RD}})^2 + p_3 \cdot L_{\mathrm{RD}}. \tag{18}$$

3.3.3. Trays

On every tray, thermodynamic equilibrium and ideal mixing is assumed. Both mole and energy balance are formulated dynamically:

$$\frac{\mathrm{d}HU_{tr,c}}{\mathrm{d}t} = F_{tr-1,c}^L - F_{tr,c}^L + F_{tr+1,c}^V - F_{tr,c}^V - y_{tr}^{\text{side stream},L} \cdot F_{tr,c}^{\text{side stream},L}, \tag{19}$$

$$\frac{\mathrm{d}U_{tr}}{\mathrm{d}t} = Q_{tr} + F_{tr-1}^L \cdot h_{tr-1}^L - F_{tr}^L \cdot h_{tr}^L + F_{tr+1}^V \cdot h_{tr+1}^V - F_{tr}^V \cdot h_{tr}^V - y_{tr}^{\text{side stream},L} \cdot F_{tr}^{\text{side stream},L} \cdot h_{tr}^L. \tag{20}$$

Therein, y_{tr} is a binary variable that can be set to 1 if a side stream exists on this tray. The side stream may be controlled with a controller (see Section 3.3.7).

Pressure drop: The pressure drop between two stages,

$$\Delta P_{tr} = P_{tr} - P_{tr-1}, \tag{21}$$

depends on the superficial vapor velocity and the hydrostatic pressure of the tray above [24, p. 463]:

$$\Delta P_{tr} = (\rho_{tr-1}^L \cdot g \cdot h_{\mathrm{cl},tr-1} + \frac{\xi}{2} \cdot (F_{tr})^2) \cdot y_{\mathrm{CON},tr} + 5 \cdot 10^2 \cdot (1 - y_{\mathrm{CON},tr}). \tag{22}$$

Again, $y_{CON,tr}$ is a binary variable that is one for all stages except for the first tray, where there is no tray above. Instead, the pressure drop is set to an arbitrary value of 500 Pa. The clear liquid height $h_{cl,tr}$ is correlated to the liquid holdup on this tray:

$$A_{\text{active}} \cdot h_{\mathrm{cl},tr} = HU_{tr}^L \cdot v_{tr}^L. \tag{23}$$

At the same time, $h_{\mathrm{cl},tr}$ is a function of froth density $\rho_{\mathrm{froth},tr}$, weir height h_{weir}, and height above the weir $h_{\mathrm{ow},tr}$ [25]:

$$h_{\mathrm{cl},tr} = \rho_{\mathrm{froth},tr} \cdot (h_{\mathrm{weir}} + h_{\mathrm{ow},tr}). \tag{24}$$

The froth density depends on the gas load, which is expressed by the superficial velocity factor [25]:

$$\rho_{\mathrm{froth},tr} = \exp\left(\pi_1 \cdot (K_{tr})^{\pi_2}\right). \tag{25}$$

The superficial velocity factor is correlated to the F-factor by

$$K_{tr} \cdot \sqrt{\rho_{tr}^{L} - \rho_{tr}^{V}} = F_{tr}. \tag{26}$$

The F-factor depends on the superficial velocity and the vapor density:

$$F_{tr} = w_{tr}^{V} \cdot \sqrt{\rho_{tr}^{V}}, \tag{27}$$

which connects the vapor flow and the vapor velocity:

$$A_{\mathrm{column}} \cdot w_{tr}^{V} = F_{tr}^{V} \cdot v_{tr}^{V}. \tag{28}$$

Liquid flow over weir: The liquid height above the weir is calculated with the Francis-Weir formula. Due to the coupling of the clear liquid height, the holdup, the froth density and the Francis-Weir formula, fulfilling all equations may only be possible if $h_{\mathrm{ow},tr}$ is smaller than zero. Using a negative height above the weir leads to numerical errors in Equation (30). Hence, we use a smooth version of a max operator to limit the actual height above the weir and use this variable in the Francis-Weir formula for a segmental weir:

$$h_{\mathrm{ow},tr}^{\mathrm{actual}} = \max\left(h_{ow,tr}, 0\right) \approx \frac{h_{\mathrm{ow},tr}}{2} \cdot \left(\frac{h_{\mathrm{ow},tr}}{\sqrt{(h_{\mathrm{ow},tr})^2 + (10)^{-9}}} + 1 \right) + (10)^{-3}, \tag{29}$$

$$\left(\frac{h_{\mathrm{ow},tr}^{\mathrm{actual}}}{0.664} \right)^{3/2} \cdot \rho_{\mathrm{froth},tr} \cdot L_{\mathrm{weir}} = V_{\mathrm{weir},tr}^{L,\mathrm{flow}}. \tag{30}$$

The last term in Eq. (29) is a small positive value of 1 mm for numerical stability. In this way, $h_{\mathrm{ow},tr}^{\mathrm{actual}}$ remains larger than 0. More on smooth approximations of non-smooth functions can, for example, be found in [26, p. 771]

Liquid flow through tray holes (weeping): Liquid may not only leave a tray over the weir, it may also flow through the holes of a tray. This is called weeping. Wijn [27] introduced a weeping factor Ω to describe the flow through the holes of a tray:

$$V_{tr}^{L,\text{flow,weep}} = \Omega_{tr}^{\text{actual}} \cdot A_{\text{active}} \cdot \varphi \cdot \sqrt{2 \cdot g \cdot h_{\text{cl},tr}}. \tag{31}$$

This weeping factor may vary between 0 and 1, depending on the fluiddynamic state of the column. For small gas loads, the weeping factor is 1 up to a certain gas load. At this point, the weeping factor starts to drop and goes to zero for high gas loads. This behavior can be described with a min operator:

$$\Omega_{tr} = \min\left(1, f_{tr}(F_{tr})\right). \tag{32}$$

Staak [28] conducted experiments to fit the parameters A_{weep}, B_{weep}, and C_{weep} in the function f_{tr}, which depends on F-factor and free area ratio φ:

$$f_{tr} = C_{\text{weep}} \cdot \exp\left(-B_{\text{weep}} \cdot \frac{F_{tr+1}}{\varphi} + A_{\text{weep}}\right). \tag{33}$$

The min operator in Eq. (32) is again reformulated to a smooth form:

$$\Omega_{tr}^{\text{actual}} = \frac{f_{tr} - 1}{2} \cdot \left(\frac{-(f_{tr} - 1)}{\sqrt{(f_{tr} - 1)^2 + (10)^{-9}}} + 1 \right) + 1. \tag{34}$$

The behavior of this smooth version is demonstrated in Figure 5 for three different values of φ. The discrete min operator is compared to the behavior of the smoothened form. It is visible that the non-smooth behavior is well described by our approximation.

3.3.4. Reactor

As Orejas [13] pointed out, there are only a few articles studying and modeling direct chlorination reactors for EDC production, namely the work of Balasubramanian et al. [29], the kinetic investigations of Szépvölgyi and Ujhidy [22] and Wachi and Morikawa [23], and two articles by Orejas [30, 13]. Balasubramanian et al. [29] studied a stirred reactor while the other authors focussed on a bubble column, which seems to be the dominating reactor type in industry nowadays [31, p. 221].

Nevertheless, this work applies a simplified dynamic, two-phase CSTR model to describe the reactor to avoid a partial differential equation system at this point. This assumption will be revisited in section 4.

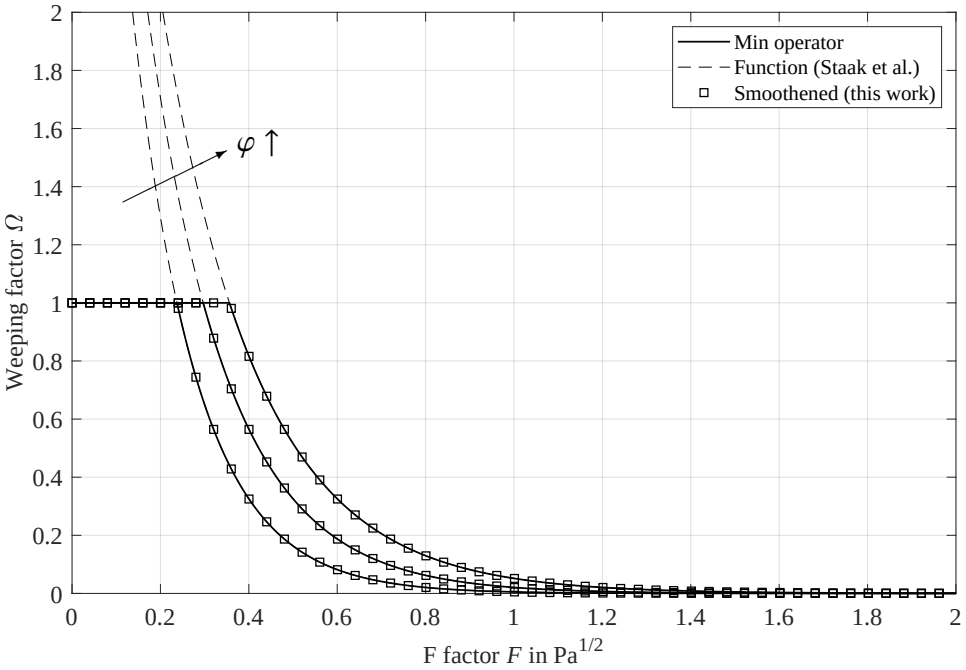

Figure 5: Weeping factor as a function of the F-factor for a free area ratio of $\varphi = \{0.1, 0.125, 0.15\}$.

Component and energy balances: The component balance includes the reactor feed, the liquid flow from the tray above $F^{L}_{tr=NTR,c}$, the liquid outlet to the heat exchanger $F^{L}_{tr=NTR+1,c}$, the vapor flow to the tray section $F^{V}_{tr=NTR+1,c}$, the reaction rates, the incoming flow from the heat exchanger $F_{HE,c}$, a possible additional flow from a secondary reactor $F_{secR,c}$ in which unreacted chlorine from the first reactor is processed, and the inlet from the heavy end removal $F^{\text{in}}_{rec,c}$:

$$\begin{aligned}\frac{\mathrm{d}HU_{c,tr=NTR+1}}{\mathrm{d}t} =& \frac{P_N \cdot V^{\text{feed, flow}}_{N,c}}{R \cdot T_N \cdot 3600} + F^{L}_{tr=NTR,c} - F^{L}_{tr=NTR+1,c} - F^{V}_{tr=NTR+1,c} \\ &+ V^{L}_{tr=NTR+1} \cdot \sum_{r=1}^{NR} \nu_{c,r} \cdot r_{tr=NTR+1,r} + F_{\text{HE},c} + F_{\text{SecR},c} \\ &+ F^{in}_{\text{rec},c} \cdot \psi_c. \end{aligned} \tag{35}$$

Therein, ψ_c indicates a simple removal factor, which is zero if a component is removed (this is true for ETC) and 1 otherwise. The expressions for the reaction rates are taken from Equations (11) and (12). The energy balance contains the

same terms as the mole balance, only the reaction does not directly appear as the heats of formation are used as reference points (see section 3.3.6). It is assumed that the flows from the secondary reactor and from the heavy end removal have the same molar enthalpy:

$$\begin{aligned}\frac{\mathrm{d}U_{tr=NTR+1}}{\mathrm{d}t} &= Q_{tr=NTR+1} + F^{\text{feed}} \cdot h^{\text{feed}} + F^{L}_{tr=NTR} \cdot h^{L}_{tr=NTR} \\ &- F^{L}_{tr=NTR+1} \cdot h^{L}_{tr=NTR+1} - F^{V}_{tr=NTR+1} \cdot h^{V}_{tr=NTR+1} + F_{\text{HE}} \cdot h_{\text{HE}} \\ &+ \left(\sum_{c=1}^{NC} F_{\text{SecR},c} + F^{\text{in}}_{\text{rec},c} \cdot \psi_c \right) \cdot h_{\text{SecR}} \end{aligned} \tag{36}$$

Pressure drop equations: Again, the same approach for the pressure drop as in the tray section is taken. However, the hydrostatic pressure of the reactor is also added.

3.3.5. External heat exchanger and heavy end removal

The heat removed in the external heat exchanger is determined by an energy balance at steady-state:

$$0 = -Q_{\text{HE}} + F^{L}_{tr=NTR+1} \cdot (h^{L}_{tr=NTR+1} - h_{HE}). \tag{37}$$

The heat flow is calculated with an overall heat transfer coefficient (OHTC, assumed value: $0.45\,\mathrm{kW\,m^{-2}\,K^{-1}}$ [32, p. 85]). The typical logarithmic temperature difference is replaced by the arithmetic mean temperature difference for numerical stability:

$$Q_{HE} = OHTC_{\text{HE}} \cdot A_{\text{HE}} \cdot \frac{\left(T_{tr=NTR+1} - T^{\text{out}}_{\text{hw}}\right) + \left(T_{\text{HE}} - T^{\text{in}}_{\text{hw}}\right)}{2}$$

The cold side of the heat exchanger is also balanced to determine the mass flow of generated hot water:

$$0 = Q_{\text{HE}} + m_{\text{hw}} \cdot c_{\text{hw}} \cdot (T^{\text{in}}_{\text{hw}} - T^{\text{out}}_{\text{hw}}). \tag{38}$$

After the heat exchanger, the outlet is split into two streams. One stream is directly recycled to the reactor (F_{HE}), the second one enters the heavy end removal ($F^{\text{in}}_{\text{rec}}$).

3.3.6. Thermodynamic Properties and Simplifications

Fugacity coefficients: Fugacity coefficients are necessary to calculate thermodynamic phase equilibria in the partial condensers, on all stages, and inside the reactor. They are calculated with the PR EoS using the binary interaction parameters estimated in Section 3.1.2.

Vapor enthalpies: Vapor enthalpies are calculated by taking the enthalpy of formation at 25 °C for the ideal gas as reference point. The temperature dependence of the ideal gas heat capacities is described by linearized forms of the hyperbolic expressions in [18, p. 2-176]:

$$h^V = \Delta_f h_c + \frac{CPA_c}{2} \cdot \left(T^2 - T_{\text{ref}}^2\right) + CPB_c \cdot (T - T_{\text{ref}}) \tag{39}$$

Enthalpy of vaporization: The enthalpy of vaporization is computed with the PR EoS: The actual expression can be found in the literature, e.g. [33, p. 339], and has been implemented for every control volume:

3.3.7. Controllers

In addition to balances and phase equilibria, the process model additionally contains controller equations. In our approach, the level in the reflux drum is controlled by the reflux. We use a PI controller for this task. The first summand is the feed-forward control to maintain the set-point, the second summand is the proportional term, and the third term contains the integral of the control deviation:

$$F_{tr=0}^{L} = F_{tr=0}^{L,\text{SP}} + K_{\text{RD}} \cdot \left(L_{\text{RD}} - L_{RD}^{\text{SP}}\right) + \frac{K_{\text{RD}}}{T_{\text{RD}}} \cdot L_{\text{RD}}^{int}. \tag{40}$$

This integral is calculated with an additional differential equation:

$$\frac{\mathrm{d}L_{\text{RD}}^{int}}{\mathrm{d}t} = L_{\text{RD}} - L_{\text{RD}}^{\text{SP}}. \tag{41}$$

The side stream on tray *tr* is coupled to the liquid volume fraction in the reactor:

$$\begin{aligned} F_{tr}^{L,\text{side stream}} = F_{tr}^{L,\text{SP,side stream}} &+ K_{tr}^{\text{side stream}} \cdot \left(\varepsilon_{tr=NTR+1}^{L} - \varepsilon_{tr=NTR+1}^{L,\text{SP}}\right) \\ &+ \frac{K_{tr}^{\text{side stream}}}{T^{\text{side stream}}} \cdot \varepsilon_{tr=NTR+1}^{L,\text{int}}, \end{aligned} \tag{42}$$

$$\frac{\mathrm{d}\varepsilon_{tr=NTR+1}^{L,\text{int}}}{\mathrm{d}t} = \varepsilon_{tr=NTR+1}^{L} - \varepsilon_{tr=NTR+1}^{L,\text{SP}}. \tag{43}$$

The coupling of the side stream to the volume fraction of the liquid phase in the reactor turned out to be the most reliable solution. However, a more realistic control setup would be using the liquid level or the hydrostatic pressure of the reactor. Finally, a P controller is used to controller the outlet temperature of the heat exchanger on the process side via the the mass flow of the hot water. Originally, all

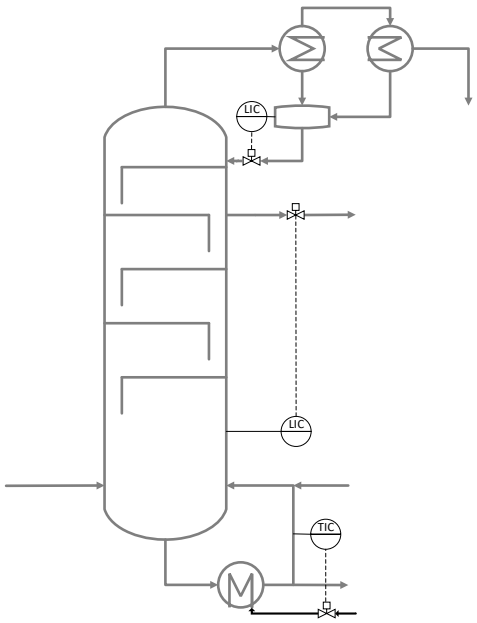

Figure 6: Process control scheme.

controllers were intended to be P controllers to keep the control structure as simple as possible. However, it was necessary to use PI controllers for both product stream and level control in the reflux drum to mimic the oscillating behavior of the obtained real plant data. In the future, these controllers will be replaced by control actions determined by optimization.

$$m_{\mathrm{hw}} = m_{\mathrm{hw}}^{\mathrm{SP}} + K_{\mathrm{hw}} \cdot (T_{\mathrm{HE}} - T_{\mathrm{HE}}^{\mathrm{SP}}) \,. \tag{44}$$

The assumed process control scheme is shown in Figure 6.

3.4. Implementation

In addition to the described dynamic model, a steady-state model was also formulated. As its main difference compared to the dynamic one are the absence of time derivatives and its lack of controller equations, the model is not presented here, but it can be deduced from the dynamic model. As part of this work, both steady-state and dynamic model have been implemented in MOSAICmodeling, a web-based modeling, simulation, and optimization environment [34, 35]. Using its code generator for various programming languages and modeling environ-

ments, the steady-state system is exported to AMPL [36] and solved with IPOPT [37], while the dynamic system is exported to the gPROMS model builder [38].

4. Simulation Results

In the following section, the results of steady-state and dynamic simulations are presented and they are compared to real plant data.

4.1. Case Study: Dynamic Tray Model

To demonstrate the performance of the dynamic tray model and the applied relaxations presented in section 3.3.3, we begin this section with a small case study, in which we demonstrate the system's response to a decrease and a subsequent increase of the vapor flow from the reactor section. This is added to (i) demonstrate the advantages of the presented modeling approach and (ii) present a small study with actual physical units as the model validation in the following section is carried out with normalized variables.

The design specifications of the case study are shown in Table 2 while the feed specifications are given in Table 3. The system is initialized at steady-state, which yields consistent initial conditions. For this case study, the reflux from the condenser is assumed to be pure EDC while the vapor flow from the reactor contains unreacted chlorine and ethene, as well as some ETC and HCl. This vapor flow rate is now continuously reduced and then increased again while the feed composition is kept constant (Figure 7). A possible explanation for such a scenario is, for example, a failing reboiler. For this simple example, we consider a column with 5 trays. The resulting pressure profile is shown in Figure 8. As the vapor flow rate from the bottom decreases, the pressure on the lower trays drops towards the fixed column pressure of 1.5 bar. This is an important difference to conventional dynamic simulations in which the pressure profile is always assumed to be given or fixed. There are two phases in the profiles: First, the pressure decreases slowly (time between 0 and 0.5 h). After 0.5 h, the pressure drops to the top pressure within a few minutes, as the single trays run dry in this time period (not shown here). In addition, the liquid height above the weir goes to zero due to the low gas load (Figure 9). At this point, conventional formulations of the Francis weir formula would not converge anymore, as the variable becomes negative. Our formulation avoids this issue by using the bounded liquid height in the Francis weir formula. In this way, our model can be solved dynamically for decreasing loads as well. The decrease in the liquid height above the weir results in a drop of the liquid volume flow above the weir, which disappears completely after 0.5 h

Table 2: Design specifications (case study).

Variable	Value	Unit
κ	0.1	–
$\rho^L_{tr=0}$	1175	kg m^{-3}
ξ	300	–
A_{active}	1	m^2
A_{column}	1.2	m^2
L_{weir}	1	m
$P_{tr=0}$	1.5	bar
V_{tr}	2.5	m^3
h_{weir}	0.04	m

Table 3: Feed specifications (case study).

Variable	Value	Unit
$F^L_{tr=0}$	50	mol s^{-1}
$F^L_{tr=0,c=3}$	50	mol s^{-1}
$F^V_{tr=6}$	51.100 02	mol s^{-1}
$F^V_{tr=6,c=1}$	1	mol s^{-1}
$F^V_{tr=6,c=2}$	0.1	mol s^{-1}
$F^V_{tr=6,c=3}$	50	mol s^{-1}
$F^V_{tr=6,c=4}$	10^{-5}	mol s^{-1}
$F^V_{tr=6,c=5}$	10^{-5}	mol s^{-1}
$F_{tr=6}$	1.85	Pa$^{0.5}$

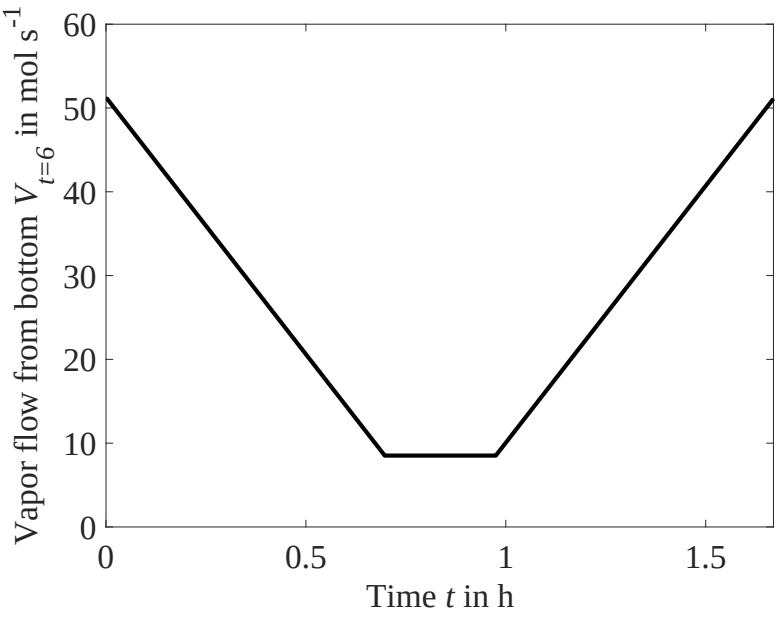

Figure 7: Profile of the feed vapor flow entering the column at the bottom.

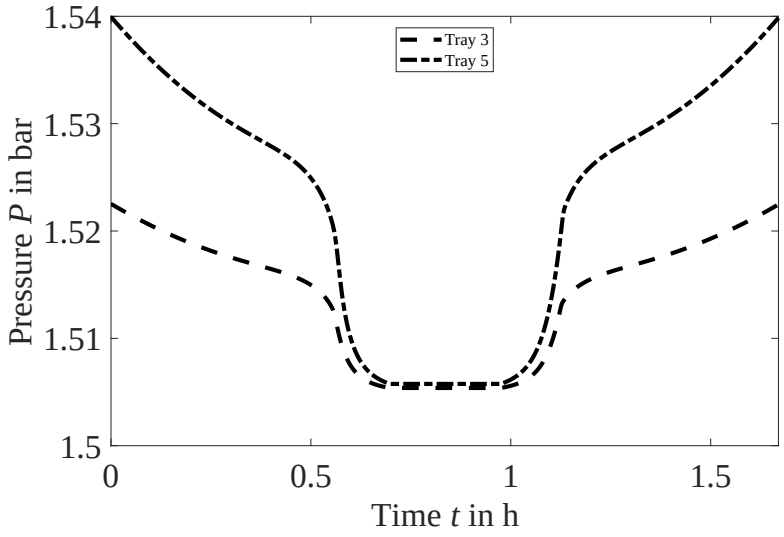

Figure 8: Profile of the pressure on tray 3 and tray 5.

and rises again as soon as the vapor flow is increased again. At the same time, the liquid volume flow by weeping increases notably with decreasing gas load (Figure 10). Note that there is always a maximum in the profiles on all trays, but with varying amplitude. This maximum can be explained by two influences on the weeping: On the one hand, weeping is increased by the weeping factor, which increases with decreasing gas load; on the other hand, weeping depends on the height of clear liquid on the tray. The weeping increases while the weeping factor still grows exponentially. As soon as it reaches its steady value of 1, weeping cannot increase anymore and reaches an equilibrium between liquid entering the tray from above and the liquid weeping through the holes.

4.2. Steady-State Results

The previous case study demonstrated the successful implementation of a pressure-driven dynamic model for a tray column. The complete model of section 3 is now solved at steady-state and in the dynamic case and its results are compared to real plant data. As stated above, all profiles are normalized as they are compared to real process data.

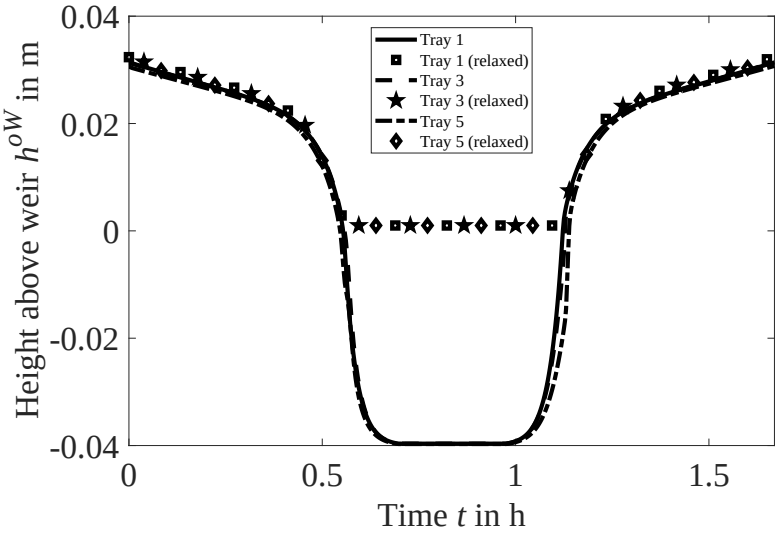

Figure 9: Profile of the liquid height above the weir on tray 1, 3, and 5. The relaxed variable is printed without a line for visual clarity.

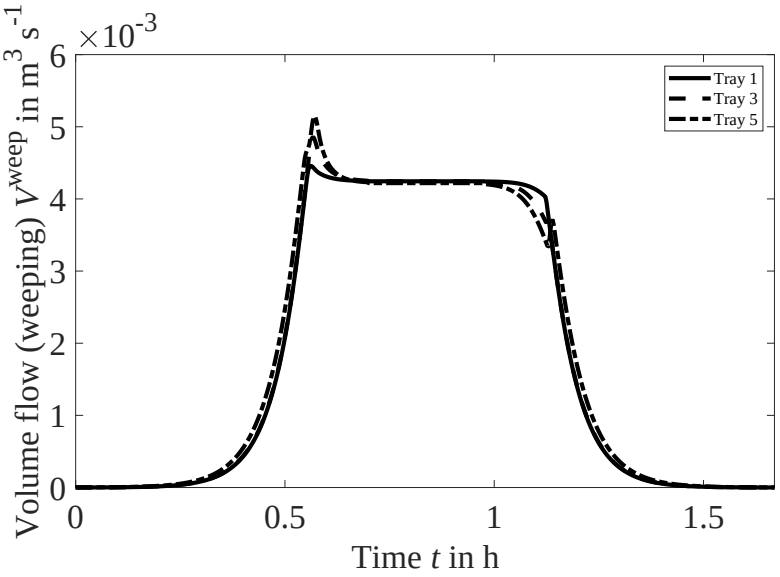

Figure 10: Profile of the liquid volume flow (weeping) on tray 1, 3, and 5.

4.2.1. Enhancement of Reaction

Early in the model development, it was evident that temperature and pressure profiles on the trays can be well described. However, when comparing the model results to real plant data, the hot water stream in the bottom heat exchanger and the liquid reflux at the top could not be matched as can be seen in Table 4. The reflux from the condenser was about 13 % smaller than in the real plant while a lot of heat had to be removed in the bottom heat exchanger. The increased heat removal is attributed to the larger pressure – and, consequently, temperature – in the reactor. It was deduced that the reaction rate in the model was smaller than in the real plant due to the assumptions of a CSTR and thermodynamic equilibrium at the bottom of the reactor. If the reaction is not fast enough, the released heat of reaction is too small to evaporate enough liquid and the conversion is too small. Hence, the hydrostatic pressure in the reactor increases and thus its temperature. This leads to an increase of Q_{HE}, which is governed by the temperature difference of process medium and water. This effect was studied by multiplying the main reaction rate with an enhancement factor β. Varying this value between 1 and 30 leads to the results given in Table 4 to Table 7. It is obvious that simply increasing the reaction rate improves the calculated reflux, but the deviation in the hot water flow, which cools the process stream in the external heat exchanger, increases again for larger values of β. Due to these observations, a value of $\beta = 10$ is used in the remainder of this work. This is the only model parameter, which was adapted to the plant data.

Additionally, it must be pointed out that increasing β to 10 does not influence the temperature (Figure 11) or pressure profile (Figure 12) over the normalized tray number (0 = condenser), because the pressure drop on the trays is virtually identical and the vaporized EDC is fairly pure (vapor mole fraction $> 97\,\%$) in all cases. Comparing the results in Figure 11 and Figure 12 with the temperature and pressure profile of the plant at nominal operating point, it becomes obvious that it is currently not possible to match both temperature and pressure profiles perfectly, but model and plant are generally in good agreement. This is an aspect, which can certainly be improved in the future, e.g. by dropping the assumption of a CSTR or by modeling the reactor as plug flow or bubble column reactor with spatial discretization. This effect is possibly enlarged by an incorrect temperature dependence of the reaction rates. The parameters taken from Orejas [13] were only reported for temperatures up to 340 K and showed a large variation. In addition, they differ significantly from the values reported by Szépvölgyi and Ujhidy [22].

Table 4: Relative deviation between real plant and model with $\beta = 1$.

Variable	Deviation
T_{HE}	$-0.4\,\%$
$F^{L}_{t=0}$	$-13.2\,\%$
m_{hw}	$62.1\,\%$
Q_{HE}	$65.0\,\%$

Table 5: Relative deviation between real plant and model with $\beta = 10$.

Variable	Deviation
T_{HE}	$-0.9\,\%$
$F^{L}_{t=0}$	$-3.9\,\%$
m_{hw}	$-0.7\,\%$
Q_{HE}	$1.1\,\%$

Table 6: Relative deviation between real plant and model with $\beta = 20$.

Variable	Deviation
T_{HE}	$-1.0\,\%$
$F^{L}_{t=0}$	$-2.7\,\%$
m_{hw}	$-7.6\,\%$
Q_{HE}	$-6.0\,\%$

Table 7: Relative deviation between real plant and model with $\beta = 30$.

Variable	Deviation
T_{HE}	$-1.0\,\%$
$F^{L}_{t=0}$	$-2.0\,\%$
m_{hw}	$-12.3\,\%$
Q_{HE}	$-10.7\,\%$

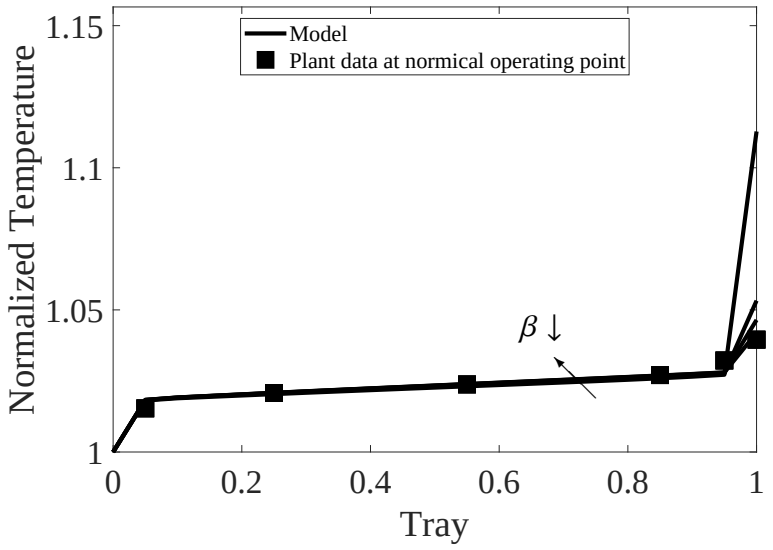

Figure 11: Normalized temperature for varying kinetic enhancement factor $\beta = 1$, 10, 20, and 30. The temperature is normalized with the condenser temperature. The feed gas load is at 100 % of the nominal gas load.

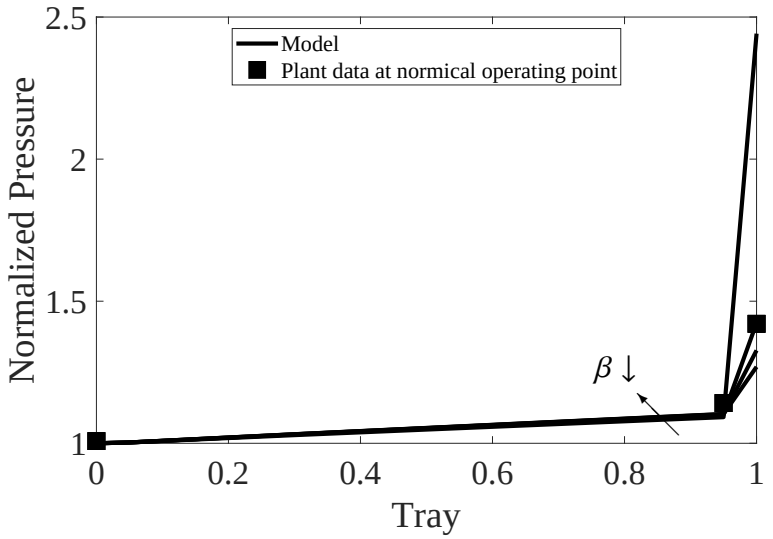

Figure 12: Normalized pressure for varying kinetic enhancement factor β = 1, 10, 20, and 30. The pressure is normalized with the condenser pressure. The feed gas load is at 100 % of the nominal gas load.

4.2.2. Steady-State Profiles

In the following, the steady-state profiles of the EDC production unit are looked at more closely for varying feed flows. As the data are compared to real plant data, all results are normalized.

The liquid height above the weir is shown in Figure 13 over the normalized tray number (0 = condenser). As expected, it decreases for decreasing feed gas load. The drop at approximately one third of the column is due to the side stream, in which liquid EDC is removed. At loads below 70 %, there is a superlinear drop; and for 50 %, all trays are essentially dry. This result is of high importance regarding flexibilization as this region should be avoided whenever possible. At such low loads, weeping increases by a factor of 100 compared to the nominal load.

In Figure 14, the normalized pressure profile is presented and compared to the steady-state profile of the plant at nominal conditions. The pressure profile shows good agreement between model and plant data, only the pressure drop on the trays is underestimated by 3.5 %. In addition, the change of the pressure drop with decreasing gas load is shown. In this case, the gas load on the trays is reduced and the pressure profile flattens out.

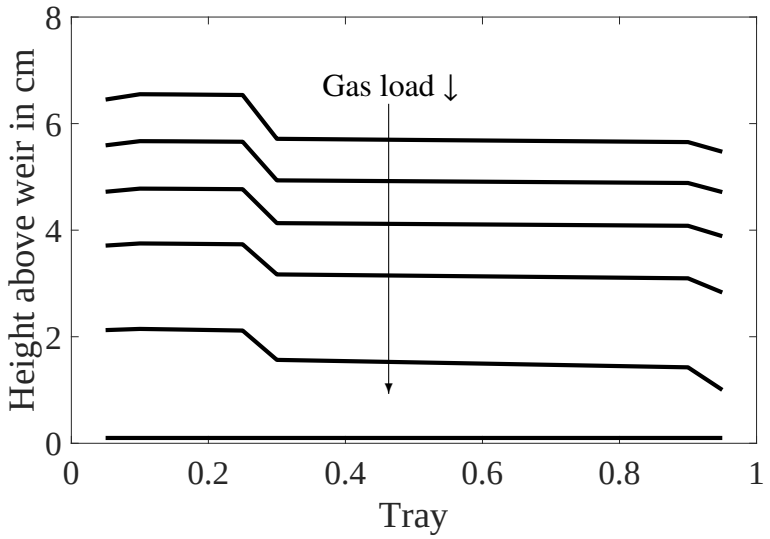

Figure 13: Liquid height above the weir for 100, 90, 80, 70, 60, and 50 % of the nominal feed load.

The normalized temperature profile is shown in Figure 15. For 100 % of feed gas load, the real plant data are also shown. Model and real data show an excellent correspondence. The largest deviations appear in the reactor section. Again, this is attributed to the simplified model of the reactor, which leads to deviations of about 5 %.

4.3. Dynamic Results

In the last section, the obtained dynamic results are analyzed and compared to real plant data. For this purpose, 24 h of a plant operation in November 2017 were simulated. Typically, the plant operates at steady-state throughout the year. However, during this period, some changes in the chlorine feed occured as is shown in Figure 16. The chlorine feed drops to about 87 % and is then increased to 92 %. We mimicked this case in our dynamic simulation. All dynamic measurement data was filtered and approximated linearly between single setpoints, which yields a reasonably accurate feed profile.

The resulting temperature profile is shown in Figure 17. In agreement with the steady-state results, deviations in the middle of the column are very small. Slightly larger deviations are observed closer to the top and the bottom. The maximum error is 3.5 %. The pressure profile is shown in Figure 18. In the reactor,

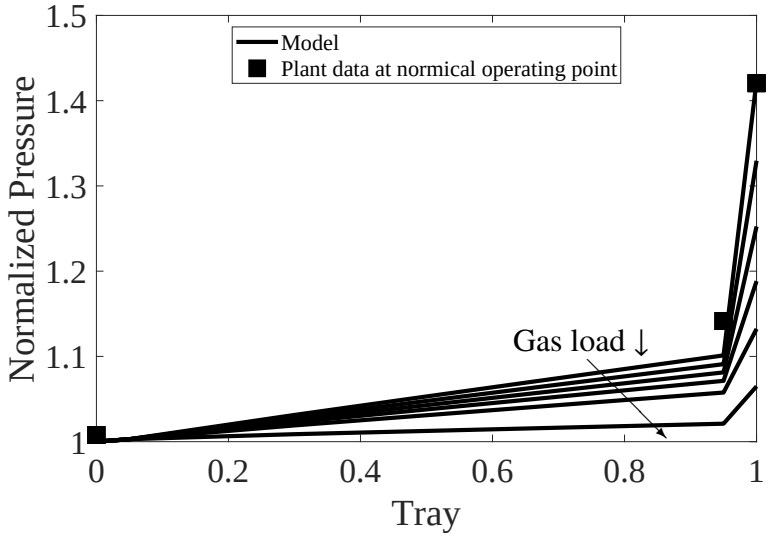

Figure 14: Normalized pressure for 100, 90, 80, 70, 60, and 50 % of the nominal feed load. The pressure is normalized with the condenser pressure.

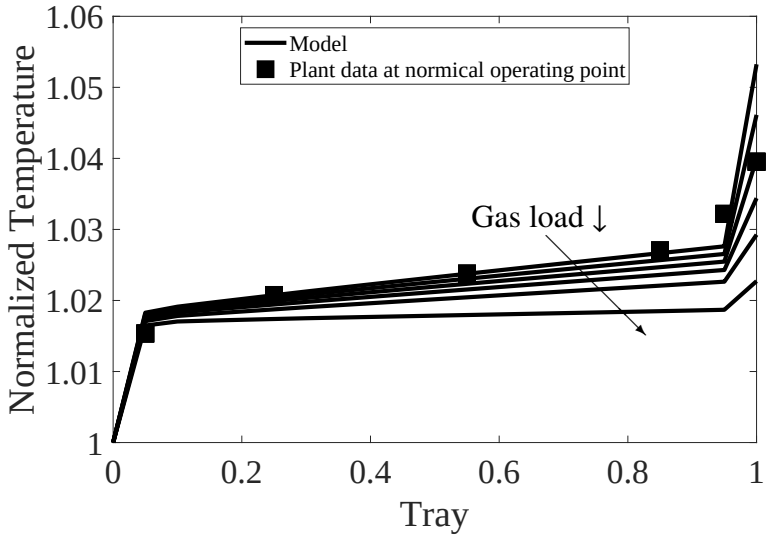

Figure 15: Normalized temperature for 100, 90, 80, 70, 60, and 50 % of the nominal feed load. The temperature is normalized with the condenser temperature.

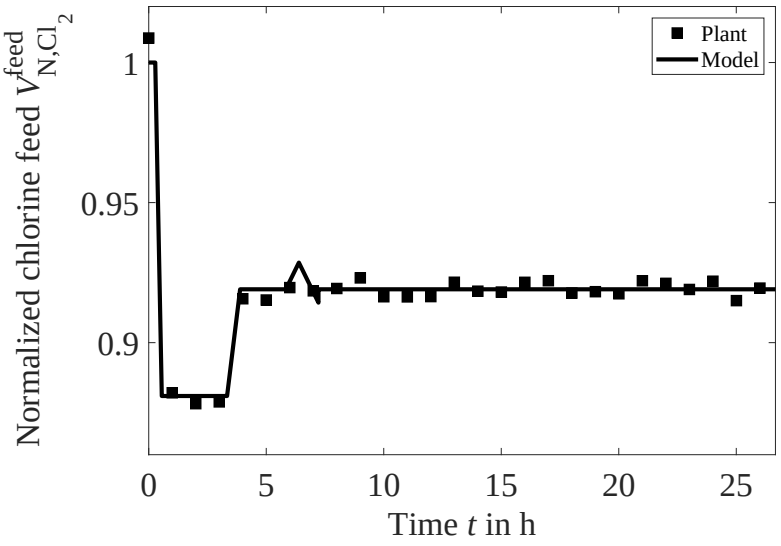

Figure 16: Normalized chlorine feed over time. The clorine feed is normalized with its nominal setpoint.

fluctuations of the hydrostatic pressure can be observed, which will be correlated to the side stream in the next figure. Similarly to the steady-state results, the pressure profile is well described with small deviations for the pressure above the reactor. The maximum error is 3.5 %. Both temperature and pressure profile are almost independent from the feed gas load, which is confirmed by the plant data and has already been pointed out in section 4.2.1.

Figure 19 presents the resulting product flow, i.e. the side stream of liquid EDC. Using the PI controller introduced in section 3.3.7, the fluctuations in the product outlet can be well described, although the frequency in the model is higher than in the real plant. This is attributed to effects, such as sample time for an industrial process control system. This will always lead to lower frequencies than in the numerical model, in which the current value of the controlled variable is directly fed back to the controller without noise. Moreover, a perfect match in the controller behavior is not necessary as the controllers will be removed from the model in the future. Instead, optimized trajectories between setpoints will be obtained using an optimization approach and the presented process model, in which the controls are degrees of freedom in the optimization problem.

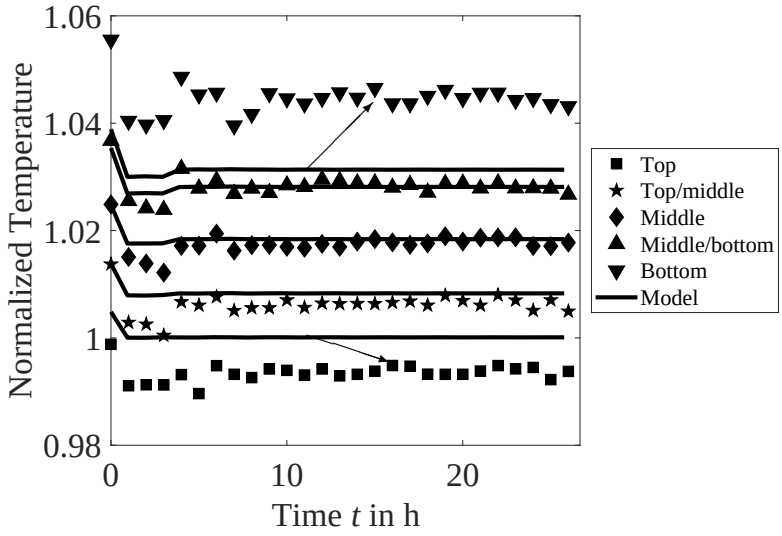

Figure 17: Normalized temperature over time. The temperature is normalized with the condenser temperature.

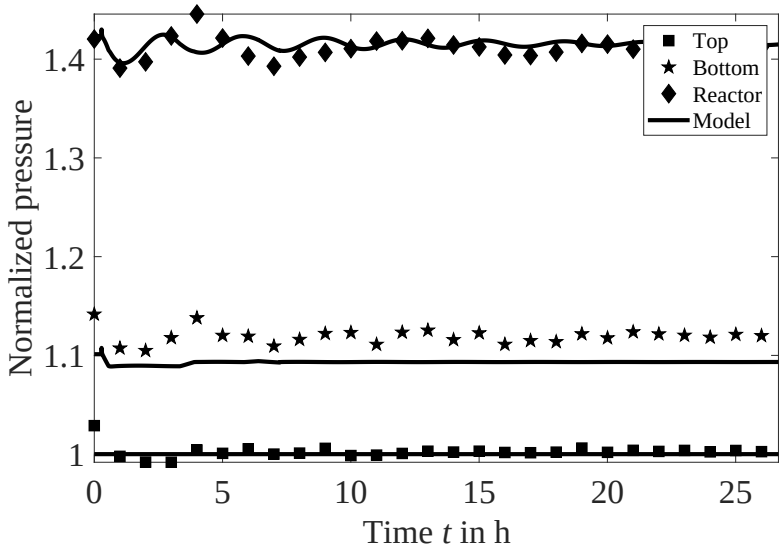

Figure 18: Normalized pressure over time. The pressure is normalized with the condenser pressure.

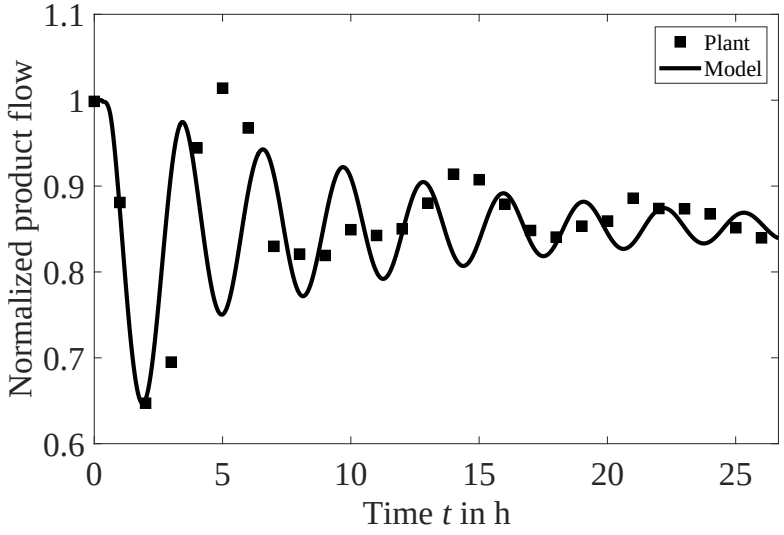

Figure 19: Normalized product flow over time. The product flow is normalized with its nominal setpoint.

5. Conclusion and Outlook

In this contribution, demand-side management was introduced as a countermeasure regarding electricity grid instabilities. In order to assess the real potential of demand-side management, the ChemEFlex project investigates technical and economical limitations for the chlor-alkali electrolysis and its downstream processes. For this purpose, a dynamic, pressure-driven model of the direct chlorination of ethene was formulated. This model consists of the reactor section, the tray section, two condensers, the reflux drum, and the peripheral units at the bottom. The model considers weeping and the flow over the weir for the liquid outlet of a tray, whereas the vapor flow is pressure-driven. To avoid convergence issues in case of low gas load and dry trays, the model equations for the liquid flow were relaxed using smooth min/max operators. The effect of these reformulations was demonstrated in a small case study. Afterwards, the model was successfully validated with real plant data of an EDC production for steady-state and dynamic conditions. All accessible measurements from the real plant can be reproduced with a maximum deviation of 5 %; in addition, we can show that stages start running dry at gas loads below 70 % of the nominal operating conditions.

Although the assumption of a CSTR for the reactor section should satisfying

results for both steady-state and dynamic simulations using a kinetic enhancement factor, modeling the reactor as plug flow or bubble column reactor will be considered. All disregarded effects of such spatially distributed units are lumped into this enhancement factor and are subject to future research. In addition, the dynamic tray model will be further expanded as there are still many aspects uncovered in this approach, e. g. the downcomer holdup, entrainment, heat and mass transfer, etc.

In the future, we will use the presented process model to determine optimal trajectories for the plant from one operating point to the other under demand response scenarios. Therein, we we will focus on day-ahead and balancing markets. These trajectories will be used to investigate any undesired concentration, temperature, or pressure profiles during the transition. Secondly, the obtained trajectories may serve as ramp constraints in a simplified linear model.

Acknowledgements

The authors acknowledge the financial support by the Federal Ministry of Economic Affairs and Energy of Germany in the project ChemEFlex (project number 0350013A).

Abbreviations

CAE	Chlor-alkali electrolysis
CSTR	Continuously stirred tank reactor
EDC	Ethylene dichloride
EoS	Equation of state
ETC	Ethylene trichloride
HCl	Hydrogen chloride
HTC	High-temperature chlorination
LTC	Low-temperature chlorination
PR	Peng-Robinson
PVC	Polyvinyl chloride
SRK	Soave-Redlich-Kwong
VCM	Vinyl chloride monomer

Greek Symbols

α	Parameter in Peng-Robinson EoS
β	Kinetic enhancement factor

δ	Binary interaction parameter
ϕ	Fugacity coefficient
φ	Free area ratio
Δ	Difference
ρ	Mass density
Ω	Weeping factor
ω	Acentric factor
ξ	Drag coefficient
ε	Volume fraction

Latin Symbols

A	Area
a	Cohesion parameter in PR-EoS
b	Covolume parameter in PR-EoS
c	Molar concentration
E	Activation energy
F	Mole flow
F	F factor
g	Gravitational acceleration
h	Molar enthalpy
h	Height
HU	Holdup
K	Gas velocity factor
K	Proportional constant of P controller
k	Pre-exponential factor in reaction kinetics
L	Length
M	Molecular weight
m	Mass flow
$OHTC$	Overall heat transfer coefficient
P	Pressure
p	Parameter for volume correlation
Q	Heat flow
R	Universal gas constant
r	Reaction rate
T	Temperature
T	Integration time of PI controller
U	Internal energy
V	Volume or volume flow (with superscript flow)
v	Molar volume

w	Superficial velocity
y	Binary variable
Indices	
c	Component index $\in [1 \dots NC]$
$caux$	Auxiliary component index $\in [1 \dots NC]$
tr	Tray index $\in [1 \dots NTR]$
Subscripts	
active	Active area
C	Critical
cl	Clear liquid
column	For the column
CON	Condenser
f	Formation
froth	Of the froth
HE	Heat exchanger
hw	Hot water
mix	Mixture
N	Norm
ow	over weir
RD	Reflux drum
rec	Recover
ref	Reference
weir	Of the weir
Superscripts	
actual	Relaxed variable
feed	Of the feed
flow	Of the flow
in	Inlet
int	Integral part of a controller
L	Liquid
side stream	Side stream
out	Outlet
Ph	Phase V or L
reactor	Of the reactor
SP	Setpoint
V	Vapor
VL	Vapor-liquid, e.g. enthalpy difference between V and L
weep	Weeping

References

[1] REN21, Renewables 2018 Global Status Report, Technical Report, Paris: REN21 Secretariat, 2018.

[2] Q. Zhang, I. E. Grossmann, Planning and Scheduling for Industrial Demand Side Management: Advances and Challenges, Springer International Publishing, Cham, 2016, pp. 383–414. URL: https://doi.org/10.1007/978-3-319-28752-2_14. doi:10.1007/978-3-319-28752-2_14.

[3] M. Baldea, Employing Chemical Processes as Grid-Level Energy Storage Devices, Springer International Publishing, Cham, 2017, pp. 247–271. URL: https://doi.org/10.1007/978-3-319-42803-1_9. doi:10.1007/978-3-319-42803-1_9.

[4] F. Ausfelder, A. Seitz, S. von Roon, Flexibilitätsoptionen in der Grundstoffindustrie: Methodik, Potenziale, Hemmnisse. Report of the Kopernikus project SynErgie, Technical Report, Dechema, 2018.

[5] S. Kohler, A.-C. Agricola, H. Seidl, dena-Netzstudie II, Technical Report, Deutsche Energie-Agentur GmbH, 2010.

[6] F. Klaucke, T. Karsten, F. Holtrup, E. Esche, T. Morosuk, G. Tsatsaronis, J.-U. Repke, Demand Response Potenziale in der chemischen Industrie, Chemie Ingenieur Technik 89 (2017) 1133–1141. doi:10.1002/cite.201600073.

[7] T. Budiarto, E. Esche, J. Repke, E. Leksono, Dynamic model of chloralkali membrane process, Procedia Engineering 170 (2017) 473–481. doi:10.1016/j.proeng.2017.03.076.

[8] J. I. Otashu, M. Baldea, Demand response-oriented dynamic modeling and operational optimization of membrane-based chlor-alkali plants, Computers & Chemical Engineering 121 (2019) 396–408. doi:10.1016/j.compchemeng.2018.08.030.

[9] L. C. Brée, K. Perrey, A. Bulan, A. Mitsos, Demand side management and operational mode switching in chlorine production, AIChE Journal 65 (2018) e16352. doi:10.1002/aic.16352.

[10] Verband der chemischen Industrie e.V., Chemiewirtschaft in Zahlen 2018, Technical Report, Verband der chemischen Industrie e.V., 2018.

[11] I. Fischer, W. F. Schmitt, H.-C. Porth, M. W. Allsopp, G. Vianello, Poly(Vinyl Chloride) in: Ullmann's Encyclopedia of Industrial Chemistry, Wiley-VCH Verlag GmbH & Co. KGaA, 2014. doi:10.1002/14356007.o06_o01.pub2.

[12] S. Sass, A. Mitsos, Optimal operation of dynamic (energy) systems: When are quasi-steady models adequate?, Computers & Chemical Engineering 124 (2019) 133–139. doi:10.1016/j.compchemeng.2019.02.011.

[13] J. A. Orejas, Model evaluation for an industrial process of direct chlorination of ethylene in a bubble-column reactor with external recirculation loop, Chemical Engineering Science 56 (2001) 513–522. doi:10.1016/s0009-2509(00)00255-4.

[14] E.-L. Dreher, K. K. Beutel, J. D. Myers, T. Lübbe, S. Krieger, L. H. Pottenger, Chloroethanes and Chloroethylenes in: Ullmann's Encyclopedia of Industrial Chemistry, Wiley-VCH Verlag GmbH & Co. KGaA, 2014. doi:10.1002/14356007.o06_o01.pub2.

[15] J. Kahsnitz, D. Polte, EP 1 857 430 B8: Improved process for direct chlorination of ethylene to 1,2-dichloroethane, 2017.

[16] G. Soave, Equilibrium constants from a modified Redlich-Kwong equation of state, Chemical Engineering Science 27 (1972) 1197–1203. doi:10.1016/0009-2509(72)80096-4.

[17] D.-Y. Peng, D. B. Robinson, A new two-constant equation of state, Industrial & Engineering Chemistry Fundamentals 15 (1976) 59–64. doi:10.1021/i160057a011.

[18] D. W. Green, R. H. Perry, Perry's Chemical Engineers' Handbook, Eighth Edition, McGraw-Hill Education, 2007.

[19] F. N. Kissell, F. S. Manning, Vapor-liquid equilibrium data for the binary mixtures carbon tetrachloride-1,1,2-trichloroethane and 1,2-dichloroethane-1,1,2-trichloroethane., Journal of Chemical & Engineering Data 7 (1962) 205–206. doi:10.1021/je60013a012.

[20] D. C. Bigg, S. C. Banerjee, L. K. Doraiswamy, Binary vapor-liquid equilibria involving 1,2-dichloroethane and 1,1,1- and 1,1,2-trichloroethane.,

Journal of Chemical & Engineering Data 9 (1964) 17–19. doi:10.1021/je60020a007.

[21] U. Westhaus, T. Dröge, R. Sass, DETHERM®—a thermophysical property database, Fluid Phase Equilibria 158-160 (1999) 429–435. doi:10.1016/s0378-3812(99)00139-9.

[22] J. Szépvölgyi, A. Ujhidy, Studies on ethylene dichloride formation in a rotary film reactor. i. kinetic investigations, Hungarian Journal of Industrial Chemistry (1978).

[23] S. Wachi, H. Morikawa, Chlorination of ethylene in a boiling bubble column reactor, Journal of Chemical Engineering of Japan 20 (1987) 238–245. doi:10.1252/jcej.20.238.

[24] J. Stichlmair, Distillation, 2. Equipment in: Ullmann's Encyclopedia of Industrial Chemistry, Wiley-VCH Verlag GmbH & Co. KGaA, 2010. doi:10.1002/14356007.o08_o01.

[25] D. L. Bennett, R. Agrawal, P. J. Cook, New pressure drop correlation for sieve tray distillation columns, AIChE Journal 29 (1983) 434–442. doi:10.1002/aic.690290313.

[26] L. T. Biegler, I. E. Grossmann, A. W. Westerberg, Systematic Methods of Chemical Process Design, Prentice Hall, 1997. URL: https://www.amazon.com/Systematic-Methods-Chemical-Process-Design/dp/0134924223?SubscriptionId=AKIAIOBINVZYXZQZ2U3A&tag=chimbori05-20&linkCode=xm2&camp=2025&creative=165953&creativeASIN=0134924223.

[27] E. Wijn, On the lower operating range of sieve and valve trays, Chemical Engineering Journal 70 (1998) 143–155. doi:10.1016/s0923-0467(98)00089-x.

[28] D. Staak, Absicherung von Destillationskolonnen im nichtbestimmungsgemäßen Betrieb, Ph.D. thesis, Technische Universität Berlin, 2010.

[29] S. N. Balasubramanian, D. N. Rihani, L. K. Doraiswamy, Film model for ethylene dichloride formation. adsorption and reaction of two gases in a liquid, Industrial & Engineering Chemistry Fundamentals 5 (1966) 184–188. doi:10.1021/i160018a006.

[30] J. A. Orejas, Modelling and simulation of a bubble-column reactor with external loop: Application to the direct chlorination of ethylene, Chemical Engineering Science 54 (1999) 5299–5309. doi:10.1016/s0009-2509(99)00254-7.

[31] A. Azapagic, S. Perdan, R. Clift (Eds.), Sustainable Development in Practice: Case Studies for Engineers and Scientists, Wiley, 2004.

[32] W. Roetzel, B. Spang, C3 Typische Werte von Wärmedurchgangskoeffizienten, Springer Berlin Heidelberg, Berlin, Heidelberg, 2013, pp. 85–90. URL: https://doi.org/10.1007/978-3-642-19981-3_7. doi:10.1007/978-3-642-19981-3_7.

[33] J. Gmehling, B. Kolbe, M. Kleiber, J. Rarey, Chemical Thermodynamics for Process Simulation, Wiley-VCH, 2012.

[34] V. A. Merchan, E. Esche, S. Fillinger, G. Tolksdorf, G. Wozny, Computer-aided process and plant development. a review of common software tools and methods and comparison against an integrated collaborative approach, Chemie Ingenieur Technik 88 (2015) 50–69. doi:10.1002/cite.201500099.

[35] E. Esche, C. Hoffmann, M. Illner, D. Müller, S. Fillinger, G. Tolksdorf, H. Bonart, G. Wozny, J.-U. Repke, MOSAIC - enabling large-scale equation-based flow sheet optimization, Chemie Ingenieur Technik 89 (2017) 620–635. doi:10.1002/cite.201600114.

[36] R. Fourer, D. M. Gay, B. W. Kernighan, AMPL: A Modeling Language for Mathematical Programming, Cengage Learning, 2002.

[37] A. Wächter, L. T. Biegler, On the implementation of an interior-point filter line-search algorithm for large-scale nonlinear programming, Mathematical Programming 106 (2005) 25–57. doi:10.1007/s10107-004-0559-y.

[38] Process Systems Enterprise, gPROMS, 1997-2018. URL: www.psenterprise.com/gproms.